NANO LETTERS

Σ3(111) Grain Boundaries Accelerate Hydrogen Insertion into Palladium Nanostructures

K. A. U. Madhushani,▽ Hyoju Park,▽ Hua Zhou, Diptangshu Datta Mal, Bingxin Yang, Qin Pang, Dongsheng Li,* Peter V. Sushko,* and Long Luo*

Cite This: https://doi.org/10.1021/acs.nanolett.5c03431 Read Online

ABSTRACT: Grain boundaries (GBs) are frequently implicated as key defect structures facilitating metal hydride formation, yet their specific role remains poorly understood due to their structural complexity. Here, we investigate hydrogen insertion in Pd nanostructures enriched with well-defined Σ3(111) GBs (Pd_{GB}) synthesized via electrolysis-driven nanoparticle assembly. *In situ* synchrotron X-ray diffraction reveals that Pd_{GB} exhibits dramatically accelerated hydriding and dehydriding kinetics compared with ligand-free and ligand-capped Pd nanoparticles with similar crystallite sizes. Strain mapping using environmental transmission electron microscopy shows that strain is highly localized at GBs and intensifies upon hydrogen exposure, indicating preferential hydrogen insertion along GB sites. Density functional theory calculations provide mechanistic insight supporting these findings, showing that hydrogen insertion near Σ3(111) GBs is energetically more favorable and that tensile strain lowers insertion barriers. These results provide atomic-level insights into the role of GBs in hydride formation and suggest new design strategies for GB-engineered Pd-based functional materials.

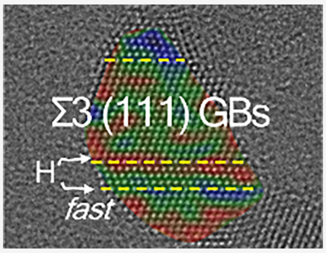

KEYWORDS: *Hydrogen Insertion, Tensile Strain, Grain Boundaries, Palladium Nanostructures*

Metal hydride formation is a critical process because it underpins a wide range of energy technologies and phenomena, including hydrogen storage,[1−3] metal-hydride electrochemical energy storage,[4−7] electrochemical energy conversion (e.g., using fuel cells),[3] chemical transformations including hydrogenation and dehydrogenation,[8,9] hydrogen gas sensing,[10−17] hydrogen purification,[18,19] and degradation of energy systems via hydrogen embrittlement.[20−24] Understanding the interaction of hydrogen with metals is also important in the context of hydrogen trapping in fusion materials and controlling plasma processing in microelectronics devices.[25−28]

Pd is widely studied for its metal−hydrogen interactions due to its high hydrogen absorption capacity and fast kinetics under ambient conditions. Early studies focused on macroscopic Pd materials, such as single crystals and polycrystalline films.[29−34] However, due to the high cost of Pd and, accordingly, the need to utilize Pd more effectively, research has shifted toward understanding hydride formation at the nanoscale, particularly the effects of the size and shape of nanoparticles (NPs). Yamauchi et al. showed that smaller Pd NPs have stronger Pd−H interactions compared with macroscopic Pd.[35] Ingham et al. confirmed similar size effects using *in situ* synchrotron X-ray diffraction (XRD),[36] while Langhammer et al. demonstrated diffusion-limited hydriding kinetics and surface tension-controlled hydrogen desorption for Pd NPs using nanoplasmonic sensing.[37] Berlinguette et al. found that lattice-strained vertices in Pd nanocrystals accelerate hydrogen uptake.[38] Meanwhile, Zlotea et al. observed a size-induced phase transition from fcc to icosahedral structures in ∼2.5 nm Pd NPs using XRD and extended X-ray absorption fine structure (EXAFS).[39] Lamberti et al. reported core−shell behavior, where a crystalline core undergoes sharp $\alpha-\beta$ transitions while an amorphous shell absorbs hydrogen gradually.[40] Dionne et al. used *in situ* scanning transmission electron microscopy (STEM) to track β-phase nucleation in Pd nanocubes, starting at corners and propagating along (100) planes, with size-dependent equilibrium pressures.[41,42] Monte Carlo simulations by Ruda et al. showed that different NP shapes lead to multiplateau behavior in pressure−composition isotherms, unlike bulk Pd.[43] Recently, interest has expanded to bimetallic systems. Kitagawa et al. used solid-state ^{2}H nuclear magnetic resonance (NMR) to show hydrogen accumulation at Pd/Pt core−shell interfaces, highlighting the role of interfacial sites in hydride stabilization.[44] Ogura et al. found that submonolayer Au alloying on Pd(110) enhances hydrogen uptake by lowering the insertion barrier, attributed to electronic effects observed via angle-resolved photoemission spectroscopy (ARPES).[45]

While the effects of particle size, shape, and composition on Pd hydride thermodynamics and kinetics are relatively well

Received: July 1, 2025
Revised: September 26, 2025
Accepted: September 29, 2025

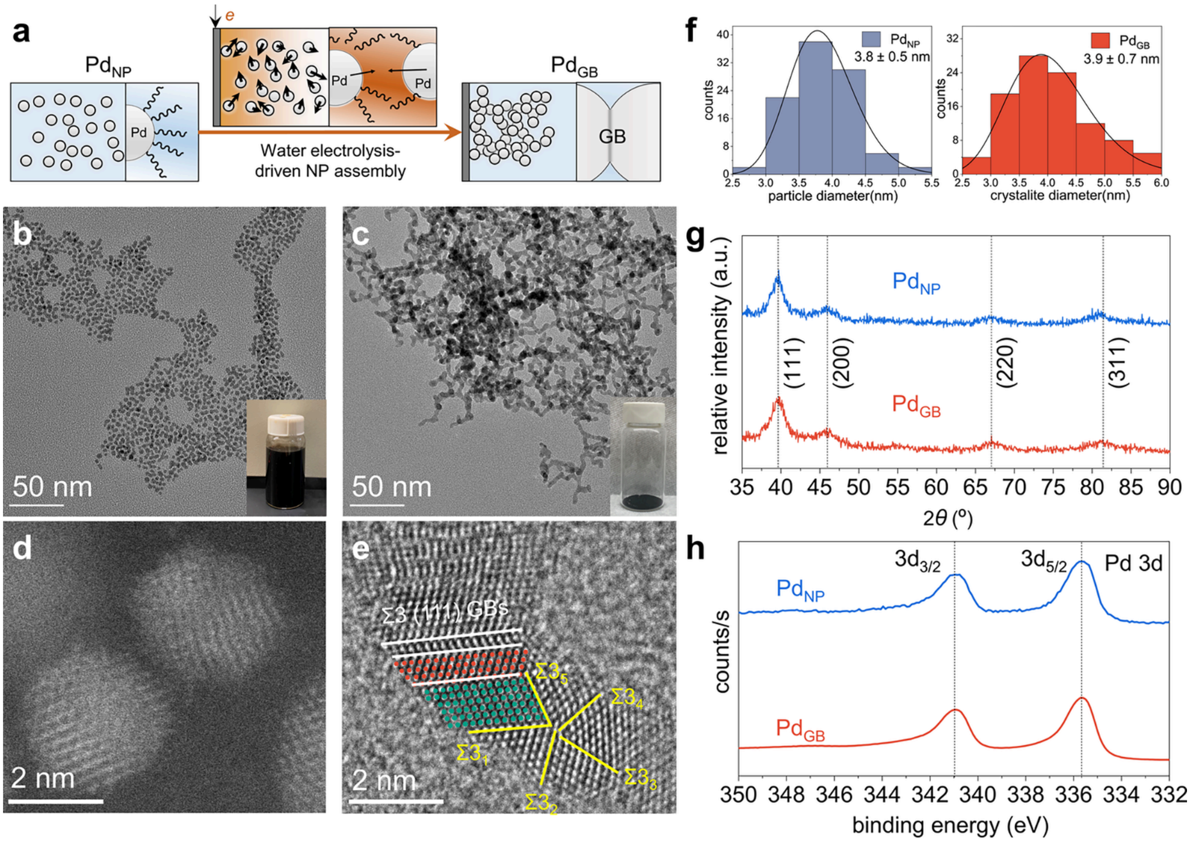

Figure 1. Synthesis and characterization of Pd nanoparticles (Pd_{NP}) and their grain boundary (GB)-rich assembly (Pd_{GB}). (a) Schematic of the water electrolysis-driven assembly of Pd_{NP} into Pd_{GB}. (b, d) TEM images of Pd_{NP}. (c, e) TEM images of Pd_{GB}, showing the prevalence of Σ3(111) GBs and 5-fold Σ3 GBs ($\Sigma 3_1$ to $\Sigma 3_5$). Red and green dots represent individual atoms in two domains separated by a Σ3(111) GB. (f) Crystallite size distributions, (g) XRD patterns, and (h) XPS spectra of Pd_{NP} and Pd_{GB}.

understood, the role of structural defects, particularly grain boundaries (GBs), remains less clear. This gap is especially notable given that GBs are often considered key sites for hydrogen absorption, diffusion, and phase transitions.[46−48]

Studying the hydride behavior at GBs is challenging due to their structural complexity. Each GB is defined by five degrees of freedom: three for grain misorientation and two for boundary plane orientation. This complexity makes it difficult to isolate specific GB types and establish clear structure−property relationships. Only a few studies have explored this topic. For example, atomistic simulations suggest GBs in Ni promote hydride formation due to favorable hydrogen binding sites.[23] In Pd, modeling predicts enhanced hydrogen storage in GB-rich nanostructures,[49] and experimental methods like cryo-atom probe tomography[20] and plasmonic imaging[50,51] have started to link GB structures with hydride kinetics.

To address the lack of the structure−property relationships for metal hydride formation at GBs, we synthesized samples in the form of interconnected quasi-1D Pd chains with well-defined Σ3(111) GBs, which not only allow for a detailed characterization of the GB's structural changes upon hydrogenation but also enable novel responses to H uptake, using *in situ* XRD and *in situ* TEM, and complementary computational modeling. Experimentally, we observe a rapid phase transition from Pd to PdH_x and back, with strain mapping revealing localized strain at these GBs. *In situ* high resolution transmission electron microsocpy (HR-TEM) results suggest that hydrogen insertion prefers the Σ3(111) GBs over the non-GB sites, confirming their role in facilitating hydride formation. Density functional theory (DFT) calculations indicate that hydrogen preferentially accumulates near the concave sites in the vicinity of GBs and further show that tensile strain at GBs lowers the hydrogen insertion barrier.

The Pd nanostructure enriched with Σ3(111) GBs (Pd_{GB}) was synthesized via a water electrolysis-driven Pd NP (Pd_{NP}) assembly method previously developed by our group (illustrated in Figure 1a).[52] This strategy utilizes electro-generated H_2 and the localized high pH near the cathode to remove citrate ligands from Pd NPs, destabilizing them and promoting random collisions in solution.[52] These collisions result in oriented attachment predominantly at the (111) facets,[53] leading to the formation of Σ3(111) GBs.[54] The GB density in the Pd_{GB} sample was estimated to be ∼3000 μm^{-1} using an electrochemical method reported in the literature.[55]

Figure 1b−e shows TEM images and optical photographs of Pd_{NP} and Pd_{GB}. HR-TEM images in Figures 1e and S1−S3 reveal the presence of parallel Σ3(111) GBs and several 5-fold Σ3 GBs ($\Sigma 3_1$ to $\Sigma 3_5$) where five grains are arranged in a cyclic structure around a common axis (see Supporting Information (SI) for details on GB identification). The 5-fold twins are believed to form through repeated oriented attachment of NPs. This configuration promotes the creation of additional Σ3(111) GBs through high-energy GB decomposition or partial dislocation slipping.[54] Earlier studies indicated that approximately 15% of oriented attachment events in Pd NPs would result in the formation of 5-fold twins.[54] In the Pd_{GB} sample, each NP typically shares ∼2−3 GBs with its neighbors (Figure S4a,b). In contrast, we only occasionally observe a few

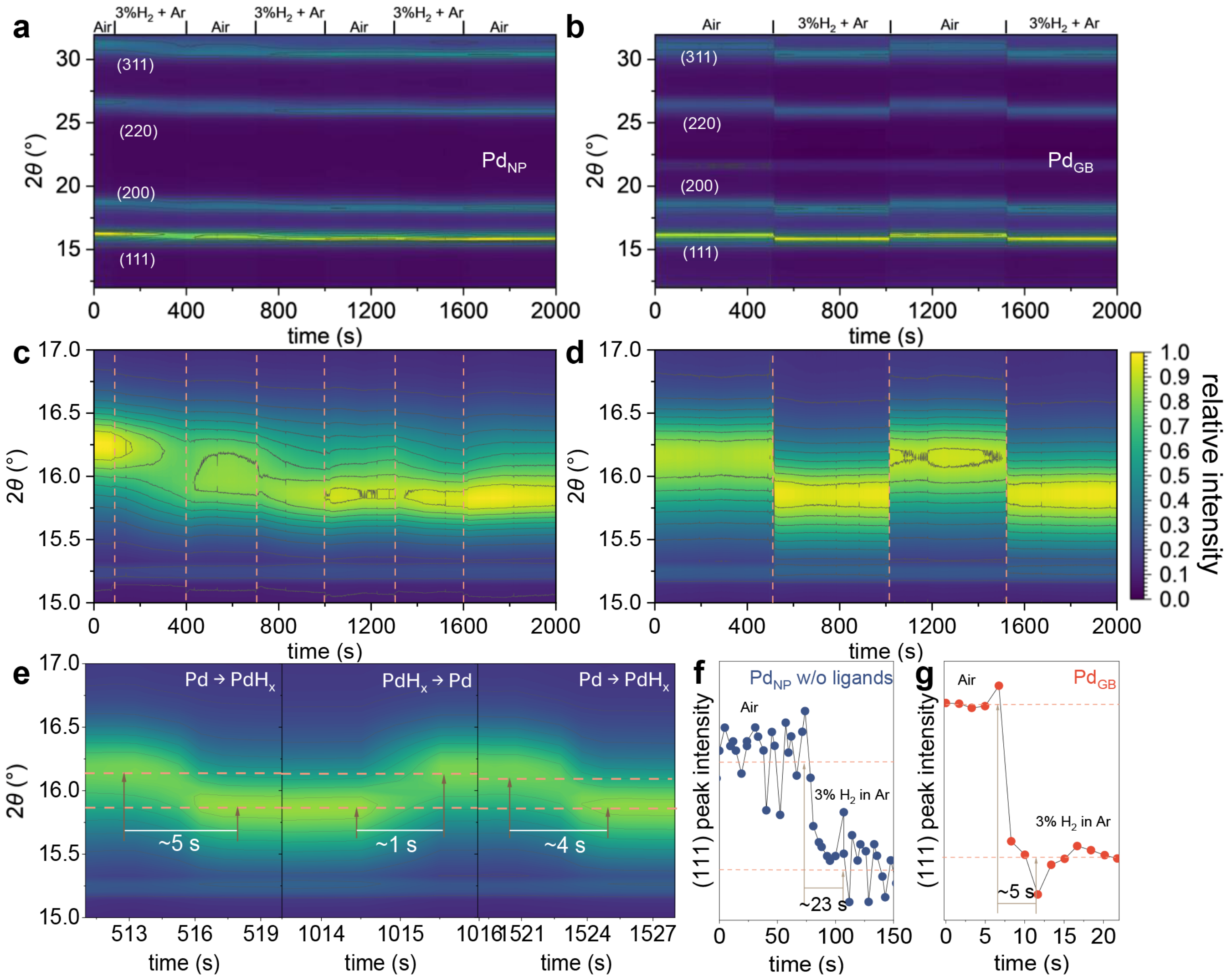

Figure 2. *In situ* synchrotron XRD analysis of hydrogen-induced phase transitions. (a, b) Time-resolved XRD patterns of Pd_{NP} and Pd_{GB} under alternating flows of air and 3% H_2 in Ar. (c, d) Enlarged views of the Pd(111) diffraction peak for Pd_{NP} and Pd_{GB}. The dashed lines indicate the switching points between air and H_2/Ar gas flows. (e) Time-resolved phase transition dynamics between Pd and PdH_x in the presence and absence of 3% H_2 in Ar for Pd_{GB}. (f, g) Comparison of the Pd(111) peak intensity changes between ligand-free Pd_{NP} and Pd_{GB} upon exposure to 3% H_2 in Ar.

GB defects in the TEM images of Pd_{NP} (Figure S4c,d). Additionally, GB-like defects were rarely observed in individual NPs. Instead, they appeared between NPs in a few small clusters

TEM-based size analysis reveals that Pd_{NP} and Pd_{GB} have similar crystallite size distributions: 3.8 ± 0.5 nm for Pd_{NP} and 3.9 ± 0.7 nm for Pd_{GB} (Figures 1f and S5). This finding is further supported by comparable XRD peak widths for both samples (Figures 1g and S6). Using the Scherrer equation, the average crystallite sizes were calculated to be 3.6 nm for Pd_{NP} and 3.8 nm for Pd_{GB} from the (220) peak of their high-resolution XRD pattern (see SI for details). The similarity in crystallite size is crucial for this study, as the rate of Pd hydride formation is known to depend strongly on particle size.[35−37] By ensuring comparable crystallite sizes, we can isolate and evaluate the influence of other structural features, such as GBs, on the hydride formation behavior. The XPS spectra of Pd 3d in Figure 1h also confirm that Pd in both samples exists in the metallic state (Pd^0).

Next, we performed *in situ* synchrotron XRD analysis to examine the transition of Pd_{NP} and Pd_{GB} to their respective hydride phases. Figure 2a,c displays the time-resolved XRD patterns of Pd_{NP} under alternating flows of air and 3% H_2 in Ar. The Pd (111) peak, initially located at ~16.2°, gradually shifted to ~16.0° after 5 min of H_2 exposure, indicating the slow formation of PdH_x. Upon switching back to air, the peak location showed minimal reversal, suggesting sluggish hydrogen desorption, likely due to citrate surface ligands on Pd_{NP} that impede hydrogen atom recombination and, consequently, hydrogen desorption. This irreversible absorption−desorption behavior resulted in a progressive, one-directional negative shift of the Pd(111) peak, stabilizing at ~15.8° after several H_2 on/off cycles. The overall lattice expansion of ~2.3% in 3% H_2 is close to the previously reported value of ~2.5% under similar conditions,[40] which corresponds to a mixed α and β phase of PdH_x. In stark contrast, Pd_{GB}, with the same mass loading of Pd as Pd_{NP}, exhibited a rapid and reversible XRD peak shift in response to gas composition changes (Figure 2b,d). As shown in Figure 2e, the Pd-to-PdH_x transition, corresponding to the

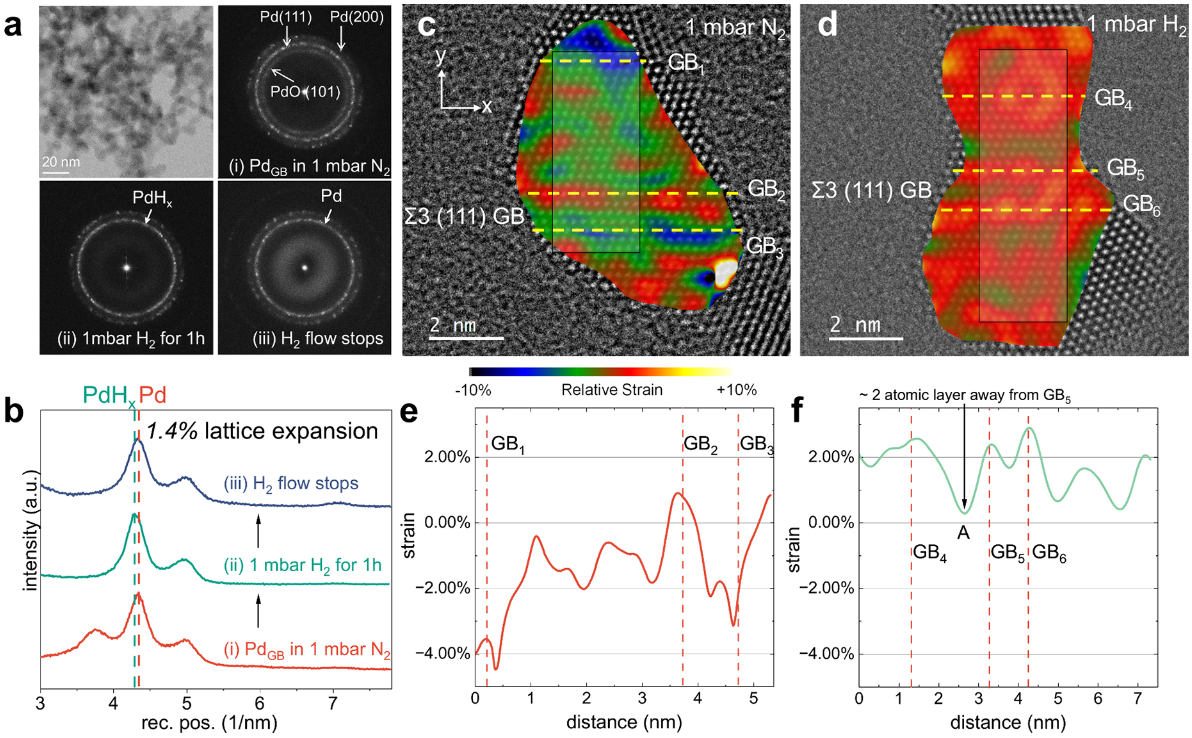

Figure 3. *In situ* environmental TEM analysis of hydrogen-induced phase transitions. (a) A TEM image and FFT patterns of Pd_{GB} under the following sequential conditions: (i) 1 mbar N_2, (ii) 1 mbar H_2, and (iii) after stopping H_2 flow. (b) Integrated intensity profiles of the FFT patterns shown in panel (a), plotted as a function of reciprocal space position. (c, d) HR-TEM images and corresponding *y*-direction strain maps of Pd_{GB} under (c) 1 mbar N_2 and (d) 1 mbar H_2. (e, f) Average strain profiles as a function of position for the boxed regions in panels (c) and (d). The minimum strain point A is ~2 atomic layers away from GB_5.

Pd(111) peak shift from 16.1° to 15.8°, was completed within ~4−5 s upon exposure to 3% H_2, and the reverse transition back to metallic Pd occurred within just 1 s after switching to air. The observed fast kinetics of Pd_{GB} cannot be attributed to PdO removal, as similarly rapid kinetics were observed even under air-free conditions (Figure S14). In addition, no significant dependence of the kinetics on Pd_{GB} loading was observed within the 50−500 μg range, which is relevant to the loading used the *in situ* XRD experiments (Figure S14a−d). The structure of Pd_{GB} did not show noticeable changes before and after multiple H_2 on/off cycles, either (Figure S15).

To isolate the effect of surface ligands on hydrogen absorption and desorption, we prepared ligand-free Pd_{NP} by treating the original citrate-capped Pd_{NP} with UV-ozone. This treatment selectively removes organic surface impurities without compromising the structural integrity of the Pd nanocrystals,[53,56] as confirmed by XRD, XPS, and TEM (Figures S7−S9). Following ligand removal, the hydrogen-induced phase transition became fully reversible (Figure S10), confirming that citrate ligands indeed inhibit hydrogen desorption. Moreover, the phase transition is significantly accelerated relative to that of the original, ligated Pd_{NP}. Figure 2f shows the change in the Pd(111) XRD peak intensity for the ligand-free Pd_{NP} upon exposure to 3% H_2 in Ar. The phase transition was completed in approximately 23 s—substantially faster than the ligated sample but still much slower than the ~5 s transition observed for Pd_{GB} (Figure 2g). These results support that Σ3(111) GBs play a key role in facilitating rapid hydrogen insertion into Pd.

To elucidate the relationship among Pd structure, Pd Σ3(111) GB content, and hydrogen insertion, we performed *in situ* TEM experiments on the Pd_{GB} sample. Figure 3a presents three sequential Fast Fourier Transform (FFT) patterns collected under 1 mbar of N_2, after 1 h of exposure to 1 mbar of H_2, and after H_2 removal. The initial FFT pattern displays three diffraction rings, corresponding to PdO(101), Pd(111), and Pd(200) (from inner to outer). The presence of PdO likely originates from the gradual surface oxidation of Pd_{GB} upon prolonged air exposure before the *in situ* TEM study. Upon H_2 exposure, the innermost ring, attributed to cubic PdO(101), disappears. The integrated FFT intensity profile in Figure 3b shows the corresponding disappearance of the ~3.745 nm^{-1} peak (*d*-spacing = 0.267 nm, tetragonal PdO(101)).[57] Simultaneously, the primary Pd(111) peak at 4.340 nm^{-1} (*d*-spacing = 0.230 nm) shifts to 4.283 nm^{-1} (*d*-spacing = 0.233 nm), indicating lattice expansion due to PdH_x formation. After the H_2 flow stops, the Pd(111) peak shifts back to its original position, confirming the reversible phase transition. The observed shift corresponds to an approximate 1.4% lattice expansion, which is higher than the previously reported value of ~0.2% for NPs with a similar size under similar H_2 pressure.[40] This discrepancy may arise due to the higher H intake by Pd_{GB}.

After confirming the reversible hydriding and dehydriding behavior of Pd_{GB} within the TEM chamber, we performed a high-resolution analysis of a region containing characteristic Σ3(111) GBs. Figures 3c and S13 show representative HR-TEM images overlaid with a *y*-direction strain map of Pd_{GB} under 1 mbar of N_2. In this region, three parallel Σ3(111) GBs (GB_1, GB_2, and GB_3) are identified in Figure 3c. GB_1 and GB_2 are separated by 15 atomic layers, whereas GB_2 and GB_3 are closer with only 4 layers between them. The strain maps were

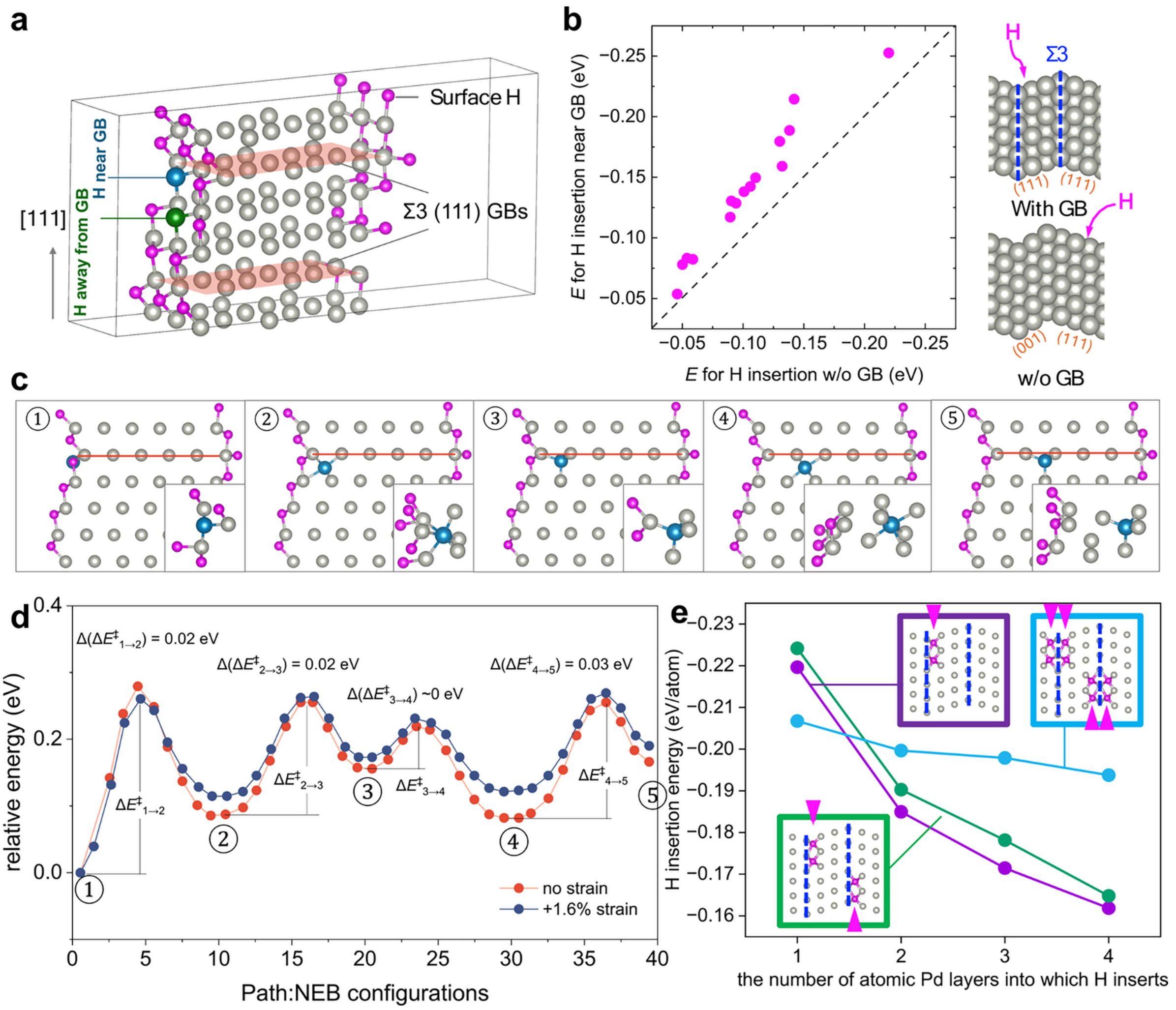

Figure 4. Mechanism of H insertion into Pd_{GB}. (a) Structural model of the GB-rich nanostructured Pd used in simulations of H insertion. Light peach plane: Σ3(111) GB; magenta: H; silver: Pd; blue: a H near a Σ3(111) GB; green: a H away from the GB. (b) Calculated energy difference for H insertion near the GB and without a GB. (c) Local atomic structures of interstitial H corresponding to the local energy minima on the calculated potential energy surface for hydrogen insertion along a Σ3(111) GB. Insets show the local coordination environment of the inserted H in each structure. (d) Potential energy profiles as a function of NEB configuration along the H insertion path with and without 1.6% tensile strain along the [111] lattice direction. In both cases, the energy of the H adsorbed on the Pd surface is set to zero. (e) Average H insertion energy depending on the number of atomic Pd layers that H inserts and insertion mode: along one plane near one GB (purple), along one plane near each GB (green), and along two planes near each GB (cyan).

generated via geometric phase analysis[58] using average experimental lattice parameters of 2.398 Å for Pd(111) and 2.087 Å for Pd(002), both measured under non-H_2 conditions at the same HR-TEM magnification. The local strain within the region ranges from approximately −7% (compressive) to +3% (tensile) with an average strain of about −1% in this TEM image. Notably, strain tends to localize at the GBs, often as a local maxima in either compression or tension. This is clearly illustrated in Figure 3d, which shows the averaged strain profile across a row of 10 Pd atoms as a function of vertical distance. The localized strain at GBs likely originates from the external forces imposed by neighboring NPs within the Pd network accumulating at the network's "connection points" (*i.e.*, GBs).

Upon exposure to 1 mbar of H_2, the Pd lattice undergoes expansion due to the hydrogen-induced phase transition. We attempted to capture this transition in real-time at the same location; however, the rapid nature of the phase change, combined with image drift at high magnification, made it challenging. As a result, we had to allow the system to equilibrate for approximately 20−30 min before acquiring new HR-TEM images. We acquired *in situ* HR-TEM images of the same region in the Pd_{GB} sample before and after hydrogen exposure (Figure S11a,b). The orientation was not ideal, preventing unambiguous identification of the GB type. Nonetheless, we observed an overall lattice expansion of ~2.3% across seven atomic layers upon exposure to H_2 flow (Figure S11c). In addition, a localized change in *d*-spacing was detected, spanning approximately one to two atomic layers adjacent to the GB (Figure S11d). During this experiment, no significant particle reorganization was observed. Unfortunately, the particle's orientation deviated from the perfect zone axis upon switching back to N_2, preventing accurate strain analysis during dehydriding.

In parallel, we also selected a nearby area containing similarly aligned parallel Σ3(111) GBs (two in close proximity to each other and the third farther away), comparable to those shown in Figure 3c, for structural comparison. Figure 3d shows its HR-TEM image overlaid with the corresponding strain map of Pd_{GB} under 1 mbar of H_2. The local strain ranges from approximately 0% (unstrained) to +4% (tensile) with an average strain of about +1%. This average strain increase upon H_2 exposure in this TEM image is consistent with the average lattice expansion of ∼1.4% observed from the FFT diffraction pattern measurements in Figure 3a,b. Most notably, the highest tensile strains of approximately +2.5% to +3% are localized at the GBs. The strain decreases rapidly with the distance from the GBs. For instance, at point A in Figure 3f, just two atomic layers away from GB_5, the strain drops sharply from ∼+2.5% at GB_5 to +0.3%. These findings clearly indicate that hydrogen preferentially inserts into Pd along the Σ3(111) GBs rather than at non-GB regions.

In addition to Σ3(111) GBs, our samples contain some other defects but at a much lower frequency, notably 5-fold twins and mismatched GBs. In a representative 5-fold-twinned region of the Pd_{GB} sample, we observed no measurable lattice expansion upon H_2 exposure (Figure S12). This may indicate either that hydride does not form along the 5-fold-twin network under our *in situ* TEM conditions or that the substantial intrinsic strain of 5-fold twins accommodates inserted H without further increasing the lattice spacing. For mismatched GBs, quantitative lattice analysis is often precluded due to orientation mismatch (adjacent NPs are seldom aligned to the same zone axis), preventing high-resolution, layer-by-layer comparison. These defects may affect hydrogen behavior and kinetics and merit a systematic study; however, the predominance of Σ3(111) GBs is likely the primary driver of the accelerated hydride formation.

The atomically well-defined Σ3(111) GB structures in Pd_{GB} enable us to construct a computational model to provide mechanistic insight into the observed behaviors. In this model, two parallel Σ3(111) GBs are separated by three atomic layers and the exposed Pd surfaces are covered with a monolayer of adsorbed hydrogen atoms (Figure 4a; see SI for details). We compared the energy required for hydrogen insertion from a surface site near a GB (blue sphere) versus one farther away (green sphere). The results show that insertion from the site farther from the GB into the first Pd sublayer is ∼0.1 eV less favorable than insertion adjacent to the GB (Figure S16). We also built a GB-free model with a nanostructure similar to that of the GB-rich model (Figure 4b). We calculated their H insertion energies for a range of configurations for comparison (Figures 4b, S17, and S18). The result in Figure 4b shows that the H insertion near a GB is consistently more favorable than that at a similar location but in the GB-free region, supporting the conclusion that GBs promote H intake, as obtained from the experimental results.

The most favorable insertion pathway follows the GB plane with the H atom alternating between tetrahedral and octahedral sites along the path (①–⑤ in Figure 4c). The highest energy barrier along the insertion pathway is ∼0.28 eV, corresponding to the first diffusion step from the surface site ① into the octahedral site ② in the first subsurface layer (Figure 4d). Transitions from octahedral to tetrahedral sites consistently show ∼0.1 eV higher barriers compared to the reverse direction (for example, $\Delta E^{\ddagger}_{2\rightarrow3}$ = 0.17 eV vs $\Delta E^{\ddagger}_{3\rightarrow4}$ = 0.06 eV), which is consistent with the higher stability of H at the octahedral sites. Our calculations also indicate that the initial H in-diffusion at the convex sites of a GB proceeds more slowly than at the concave sites of a GB (see Figures S22 and S23).

We further found that all H configurations along the diffusion path are stabilized under tensile strain and destabilized under compressive strain (Figure S20). While an expanded Pd lattice stabilizes both octahedral and tetrahedral interstitial hydrogen atoms, the rate of this effect is larger for the tetrahedral sites. Correspondingly, the energy barriers for hydrogen transfer ($\Delta(\Delta E^{\ddagger})$) are reduced by ∼0.02 to 0.03 eV under +1.6% tensile strain (Figure 4d).

Finally, we analyzed the energetics corresponding to three modalities of H insertion along the GBs (Figure 4e). Our calculations show that at the initial stages of H insertion the energy gain is high in all three cases. However, as the amount of incorporated H increases, the energy gain due to H insertion along one plane near the GB decreases sharply, while the energy gain due to H insertion along both planes near the GBs remains nearly constant. This insertion process is accompanied by an increase in the Pd–Pd interplane spacing (Figure S21). Notably, H insertion increases this *d*-spacing on both sides of the mirror planes but does not affect the lattice beyond the immediate vicinity of the GB. This localized effect of H insertion, in particular, the symmetric strain profile shown in Figure S21c, is consistent with the experimentally observed strain accumulation near the GBs (Figure 3d). Moreover, the corresponding H insertion mode, whereby H intake occurs on both sides of each GB (cyan in Figure 4e), is the most thermodynamically preferred and is consistent with the observed rapid intake of H in GB-rich Pd.

In conclusion, we examined the response of nanostructured Pd with well-defined Σ3(111) GBs (i.e., Pd_{GB}) to a hydrogen environment using *in situ* XRD and environmental TEM. Compared to Pd NPs with similar crystallite sizes (both with and without ligands), Pd_{GB} exhibited significantly faster hydriding and dehydriding kinetics, indicating that GBs facilitate hydride formation. *In situ* TEM provided microscopic insight into the role of GBs, revealing localized tensile and compressive strains at GB sites, even in the absence of H_2. Upon H_2 exposure, the tensile strain increased and remained highly localized, decaying within a couple of atomic layers of the GBs. These observations suggest that GBs serve as preferential sites for hydrogen insertion.

Computational modeling using a structurally analogous system provides further insight into the mechanisms of H insertion, effects of external strain, and character of H-induced strain distribution. The simulations showed that hydrogen insertion near the GB is energetically more favorable than at sites away from it and that tensile strain at the GBs lowers the insertion barriers by ∼0.02–0.03 eV. In addition, H insertion energetically prefers propagating along both planes near a GB. Together, these findings provide new atomic-level insights into the role of GBs in Pd hydride formation, highlight the potential of leveraging GBs to design advanced Pd-based functional materials, and offer a path for the design of high-rate H-transfer materials.

■ ASSOCIATED CONTENT

Supporting Information

The Supporting Information is available free of charge at https://pubs.acs.org/doi/10.1021/acs.nanolett.5c03431.

Chemicals and materials, general experimental methods (including the syntheses of Pd_{NP}, $Pd_{NP/UV}$, and Pd_{GB} and characterization methods), GB identification method, crystallite measurements, the ligand effect, and computational modeling details (PDF)

AUTHOR INFORMATION

Corresponding Authors

Dongsheng Li − *Physical & Computational Sciences Directorate, Pacific Northwest National Laboratory, Richland, Washington 99354, United States;* orcid.org/0000-0002-1030-146X; Email: Dongsheng.li2@pnnl.gov

Peter V. Sushko − *Physical & Computational Sciences Directorate, Pacific Northwest National Laboratory, Richland, Washington 99354, United States;* orcid.org/0000-0001-7338-4146; Email: peter.sushko@pnnl.gov

Long Luo − *Department of Chemistry, University of Utah, Salt Lake City, Utah 84112, United States;* orcid.org/0000-0001-5771-6892; Email: long.luo@utah.edu

Authors

K. A. U. Madhushani − *Department of Chemistry, University of Utah, Salt Lake City, Utah 84112, United States;* orcid.org/0000-0002-3683-6673

Hyoju Park − *Physical & Computational Sciences Directorate, Pacific Northwest National Laboratory, Richland, Washington 99354, United States*

Hua Zhou − *X-Ray Science Division, Argonne National Laboratory, Lemont, Illinois 60439, United States;* orcid.org/0000-0001-9642-8674

Diptangshu Datta Mal − *Department of Chemistry, University of Utah, Salt Lake City, Utah 84112, United States;* orcid.org/0000-0001-7584-8848

Bingxin Yang − *Department of Chemistry, University of Utah, Salt Lake City, Utah 84112, United States*

Qin Pang − *Physical & Computational Sciences Directorate, Pacific Northwest National Laboratory, Richland, Washington 99354, United States*

Complete contact information is available at: https://pubs.acs.org/10.1021/acs.nanolett.5c03431

Author Contributions

The manuscript was written through the contributions of all authors. All authors have given approval to the final version of the manuscript.

Author Contributions

$^{\nabla}$K.A.U.M. and H.P. contributed equally.

Notes

The authors declare no competing financial interest.

ACKNOWLEDGMENTS

This research was supported by the U.S. Department of Energy (DOE), Office of Science, Office of Basic Energy Sciences (BES): Materials Sciences and Engineering Division, Synthesis and Processing Science Program, FWP 78705. L.L. also gratefully acknowledges support from the University of Utah and the Alfred P. Sloan Foundation (Grant # FH-2023-20829) for the lab setup. TEM characterization was conducted in the William R. Wiley Environmental Molecular Sciences Laboratory (EMSL), a national scientific user facility sponsored by the DOE Office of Biological and Environmental Research and located at PNNL. The *in situ* XRD experiments were performed on the beamline 12-ID-D with beam time award (DOI:10.46936/APS-182977/60011131) from the Advanced Photon Source, a U.S. DOE Office of Science user facility operated for the DOE Office of Science by Argonne National Laboratory under Contract No. DE-AC02-06CH11357 and also on the beamline 4-ID of the National Synchrotron Light Source II, a DOE Office of Science User Facility operated for the DOE Office of Science by Brookhaven National Laboratory under contract no. DE-SC0012704. This work also made use of Nanofab EMSAL shared facilities of the Micron Technology Foundation Inc. Microscopy Suite sponsored by the John and Marcia Price College of Engineering, Health Sciences Center, Office of the Vice President for Research. ChatGPT was used to improve the language and clarity of the manuscript during its preparation.

REFERENCES

(1) Orimo, S.-i.; Nakamori, Y.; Eliseo, J. R.; Züttel, A.; Jensen, C. M. Complex hydrides for hydrogen storage. *Chem. Rev.* **2007**, *107* (10), 4111−4132.

(2) Sakintuna, B.; Lamari-Darkrim, F.; Hirscher, M. Metal hydride materials for solid hydrogen storage: a review. *International journal of hydrogen energy* **2007**, *32* (9), 1121−1140.

(3) Lototskyy, M. V.; Tolj, I.; Pickering, L.; Sita, C.; Barbir, F.; Yartys, V. The use of metal hydrides in fuel cell applications. *Progress in Natural Science: Materials International* **2017**, *27* (1), 3−20.

(4) Albertus, P.; Christensen, J.; Newman, J. Modeling Side Reactions and Nonisothermal Effects in Nickel Metal-Hydride Batteries. *J. Electrochem. Soc.* **2008**, *155* (1), A48−A60.

(5) Ovshinsky, S. R.; Fetcenko, M. A.; Ross, J. A Nickel Metal Hydride Battery for Electric Vehicles. *Science* **1993**, *260* (5105), 176−181.

(6) Feng, F.; Geng, M.; Northwood, D. Electrochemical behaviour of intermetallic-based metal hydrides used in Ni/metal hydride (MH) batteries: a review. *Int. J. Hydrogen Energy* **2001**, *26* (7), 725−734.

(7) Müller, T.; Friedrich, B. Development of a recycling process for nickel-metal hydride batteries. *J. Power Sources* **2006**, *158* (2), 1498−1509.

(8) Tew, M. W.; Janousch, M.; Huthwelker, T.; van Bokhoven, J. A. The roles of carbide and hydride in oxide-supported palladium nanoparticles for alkyne hydrogenation. *J. Catal.* **2011**, *283* (1), 45−54.

(9) Sanyal, U.; Yuk, S. F.; Koh, K.; Lee, M.-S.; Stoerzinger, K.; Zhang, D.; Meyer, L. C.; Lopez-Ruiz, J. A.; Karkamkar, A.; Holladay, J. D.; et al. Hydrogen Bonding Enhances the Electrochemical Hydrogenation of Benzaldehyde in the Aqueous Phase. *Angew. Chem., Int. Ed.* **2021**, *60* (1), 290−296.

(10) Koo, W.-T.; Cho, H.-J.; Kim, D.-H.; Kim, Y. H.; Shin, H.; Penner, R. M.; Kim, I.-D. Chemiresistive Hydrogen Sensors: Fundamentals, Recent Advances, and Challenges. *ACS Nano* **2020**, *14* (11), 14284−14322.

(11) Penner, R. M. A Nose for Hydrogen Gas: Fast, Sensitive H2 Sensors Using Electrodeposited Nanomaterials. *Acc. Chem. Res.* **2017**, *50* (8), 1902−1910.

(12) Koo, W.-T.; Qiao, S.; Ogata, A. F.; Jha, G.; Jang, J.-S.; Chen, V. T.; Kim, I.-D.; Penner, R. M. Accelerating Palladium Nanowire H2 Sensors Using Engineered Nanofiltration. *ACS Nano* **2017**, *11* (9), 9276−9285.

(13) Luong, H. M.; Pham, M. T.; Guin, T.; Madhogaria, R. P.; Phan, M.-H.; Larsen, G. K.; Nguyen, T. D. Sub-second and ppm-level optical sensing of hydrogen using templated control of nano-hydride geometry and composition. *Nat. Commun.* **2021**, *12* (1), 2414.

(14) Darmadi, I.; Nugroho, F. A. A.; Kadkhodazadeh, S.; Wagner, J. B.; Langhammer, C. Rationally Designed PdAuCu Ternary Alloy Nanoparticles for Intrinsically Deactivation-Resistant Ultrafast Plasmonic Hydrogen Sensing. *ACS Sensors* **2019**, *4* (5), 1424−1432.

(15) Liu, N.; Tang, M. L.; Hentschel, M.; Giessen, H.; Alivisatos, A. P. Nanoantenna-enhanced gas sensing in a single tailored nanofocus. *Nat. Mater.* **2011**, *10* (8), 631−636.

(16) Lee, J.; Shim, W.; Lee, E.; Noh, J.-S.; Lee, W. Highly Mobile Palladium Thin Films on an Elastomeric Substrate: Nanogap-Based

Hydrogen Gas Sensors. *Angew. Chem., Int. Ed.* **2011**, *50* (23), 5301−5305.

(17) Xu, T.; Zach, M. P.; Xiao, Z. L.; Rosenmann, D.; Welp, U.; Kwok, W. K.; Crabtree, G. W. Self-assembled monolayer-enhanced hydrogen sensing with ultrathin palladium films. *Appl. Phys. Lett.* **2005**, *86* (20), 203104.

(18) Rahimpour, M.; Samimi, F.; Babapoor, A.; Tohidian, T.; Mohebi, S. Palladium membranes applications in reaction systems for hydrogen separation and purification: A review. *Chemical Engineering and Processing: Process Intensification* **2017**, *121*, 24−49.

(19) Bernardo, G.; Araújo, T.; da Silva Lopes, T.; Sousa, J.; Mendes, A. Recent advances in membrane technologies for hydrogen purification. *Int. J. Hydrogen Energy* **2020**, *45* (12), 7313−7338.

(20) Chen, Y. S.; Lu, H.; Liang, J.; Rosenthal, A.; Liu, H.; Sneddon, G.; McCarroll, I.; Zhao, Z.; Li, W.; Guo, A.; et al. Observation of hydrogen trapping at dislocations, grain boundaries, and precipitates. *Science* **2020**, *367* (6474), 171−175.

(21) Li, X.; Ma, X.; Zhang, J.; Akiyama, E.; Wang, Y.; Song, X. Review of hydrogen embrittlement in metals: hydrogen diffusion, hydrogen characterization, hydrogen embrittlement mechanism and prevention. *Acta Metallurgica Sinica (English Letters)* **2020**, *33*, 759−773.

(22) Di Stefano, D.; Mrovec, M.; Elsässer, C. First-principles investigation of hydrogen trapping and diffusion at grain boundaries in nickel. *Acta Mater.* **2015**, *98*, 306−312.

(23) Song, J.; Curtin, W. A nanoscale mechanism of hydrogen embrittlement in metals. *Acta Mater.* **2011**, *59* (4), 1557−1569.

(24) Louthan, M. R.; Caskey, G. R. Hydrogen transport and embrittlement in structural metals. *Int. J. Hydrogen Energy* **1976**, *1* (3), 291−305.

(25) Benamati, G.; Donato, A.; Solina, A.; Valentini, R.; Lanza, S. Experimental studies on hydrogen diffusion and trapping in martensitic and austenitic stainless steels for fusion application. *Journal of nuclear materials* **1994**, *212*, 1401−1405.

(26) Franzen, P.; Garcia-Rosales, C.; Plank, H.; Alimov, V. K. Hydrogen trapping in and release from tungsten: Modeling and comparison with graphite with regard to its use as fusion reactor material. *Journal of nuclear materials* **1997**, *241*, 1082−1086.

(27) Serra, E.; Benamati, G.; Ogorodnikova, O. Hydrogen isotopes transport parameters in fusion reactor materials. *Journal of nuclear materials* **1998**, *255* (2−3), 105−115.

(28) Fleetwood, D. M. Effects of hydrogen transport and reactions on microelectronics radiation response and reliability. *Microelectronics Reliability* **2002**, *42* (4−5), 523−541.

(29) Gabrielli, C.; Grand, P. P.; Lasia, A.; Perrot, H. Investigation of hydrogen adsorption-absorption into thin palladium films: I. Theory. *J. Electrochem. Soc.* **2004**, *151* (11), A1925.

(30) Kay, B. D.; Peden, C. H.; Goodman, D. W. Kinetics of hydrogen absorption by Pd(110). *Phys. Rev. B Condens Matter* **1986**, *34* (2), 817−822.

(31) Michalak, W.; Miller, J.; Alfonso, D.; Gellman, A. Uptake, transport, and release of hydrogen from Pd (100). *Surface science* **2012**, *606* (3−4), 146−155.

(32) Schwarzer, M.; Hertl, N.; Nitz, F.; Borodin, D.; Fingerhut, J.; Kitsopoulos, T. N.; Wodtke, A. M. Adsorption and Absorption Energies of Hydrogen with Palladium. *J. Phys. Chem. C Nanomater Interfaces* **2022**, *126* (34), 14500−14508.

(33) Mitsui, T.; Rose, M.; Fomin, E.; Ogletree, D.; Salmeron, M. Hydrogen adsorption and diffusion on Pd (1 1 1). *Surface science* **2003**, *540* (1), 5−11.

(34) Okuyama, H.; Siga, W.; Takagi, N.; Nishijima, M.; Aruga, T. Path and mechanism of hydrogen absorption at Pd (100). *Surface science* **1998**, *401* (3), 344−354.

(35) Yamauchi, M.; Ikeda, R.; Kitagawa, H.; Takata, M. Nanosize effects on hydrogen storage in palladium. *J. Phys. Chem. C* **2008**, *112* (9), 3294−3299.

(36) Ingham, B.; Toney, M. F.; Hendy, S. C.; Cox, T.; Fong, D. D.; Eastman, J. A.; Fuoss, P. H.; Stevens, K. J.; Lassesson, A.; Brown, S. A.; et al. Particle size effect of hydrogen-induced lattice expansion of palladium nanoclusters. *Phys. Rev. B* **2008**, *78* (24), 245408.

(37) Langhammer, C.; Zhdanov, V. P.; Zoric, I.; Kasemo, B. Size-dependent kinetics of hydriding and dehydriding of Pd nanoparticles. *Phys. Rev. Lett.* **2010**, *104* (13), 135502.

(38) Johnson, N. J. J.; Lam, B.; MacLeod, B. P.; Sherbo, R. S.; Moreno-Gonzalez, M.; Fork, D. K.; Berlinguette, C. P. Facets and vertices regulate hydrogen uptake and release in palladium nanocrystals. *Nat. Mater.* **2019**, *18* (5), 454−458.

(39) Zlotea, C.; Cuevas, F.; Paul-Boncour, V.; Leroy, E.; Dibandjo, P.; Gadiou, R.; Vix-Guterl, C.; Latroche, M. Size-dependent hydrogen sorption in ultrasmall Pd clusters embedded in a mesoporous carbon template. *J. Am. Chem. Soc.* **2010**, *132* (22), 7720−7729.

(40) Bugaev, A. L.; Guda, A. A.; Lomachenko, K. A.; Shapovalov, V. V.; Lazzarini, A.; Vitillo, J. G.; Bugaev, L. A.; Groppo, E.; Pellegrini, R.; Soldatov, A. V.; et al. Core−Shell Structure of Palladium Hydride Nanoparticles Revealed by Combined X-ray Absorption Spectroscopy and X-ray Diffraction. *J. Phys. Chem. C* **2017**, *121* (33), 18202−18213.

(41) Narayan, T. C.; Hayee, F.; Baldi, A.; Leen Koh, A.; Sinclair, R.; Dionne, J. A. Direct visualization of hydrogen absorption dynamics in individual palladium nanoparticles. *Nat. Commun.* **2017**, *8* (1), 14020.

(42) Baldi, A.; Narayan, T. C.; Koh, A. L.; Dionne, J. A. In situ detection of hydrogen-induced phase transitions in individual palladium nanocrystals. *Nat. Mater.* **2014**, *13* (12), 1143−1148.

(43) Crespo, E. A.; Ruda, M.; de Debiaggi, S. R.; Bringa, E. M.; Braschi, F. U.; Bertolino, G. Hydrogen absorption in Pd nanoparticles of different shapes. *international journal of hydrogen energy* **2012**, *37* (19), 14831−14837.

(44) Kobayashi, H.; Yamauchi, M.; Kitagawa, H.; Kubota, Y.; Kato, K.; Takata, M. Hydrogen Absorption in the Core/Shell Interface of Pd/Pt Nanoparticles. *J. Am. Chem. Soc.* **2008**, *130* (6), 1818−1819.

(45) Namba, K.; Ogura, S.; Ohno, S.; Di, W.; Kato, K.; Wilde, M.; Pletikosic, I.; Pervan, P.; Milun, M.; Fukutani, K. Acceleration of hydrogen absorption by palladium through surface alloying with gold. *Proc. Natl. Acad. Sci. U. S. A.* **2018**, *115* (31), 7896−7900.

(46) Pundt, A.; Kirchheim, R. Hydrogen in metals: microstructural aspects. *Annu. Rev. Mater. Res.* **2006**, *36* (1), 555−608.

(47) Oudriss, A.; Creus, J.; Bouhattate, J.; Conforto, E.; Berziou, C.; Savall, C.; Feaugas, X. Grain size and grain-boundary effects on diffusion and trapping of hydrogen in pure nickel. *Acta Mater.* **2012**, *60* (19), 6814−6828.

(48) Delmelle, R.; Amin-Ahmadi, B.; Sinnaeve, M.; Idrissi, H.; Pardoen, T.; Schryvers, D.; Proost, J. Effect of structural defects on the hydriding kinetics of nanocrystalline Pd thin films. *Int. J. Hydrogen Energy* **2015**, *40* (23), 7335−7347.

(49) López, J.; Schmidth, W.; Roco, F.; Soto, W.; Ramírez, M.; Prada, A.; Valencia, F. J.; Varas, A.; Rogan, J. Grain boundaries improve hydrogen storage in Palladium hollow nanoparticles. *Int. J. Hydrogen Energy* **2024**, *81*, 805−811.

(50) Alekseeva, S.; Strach, M.; Nilsson, S.; Fritzsche, J.; Zhdanov, V. P.; Langhammer, C. Grain-growth mediated hydrogen sorption kinetics and compensation effect in single Pd nanoparticles. *Nat. Commun.* **2021**, *12* (1), 5427.

(51) Alekseeva, S.; Fanta, A. B. d. S.; Iandolo, B.; Antosiewicz, T. J.; Nugroho, F. A. A.; Wagner, J. B.; Burrows, A.; Zhdanov, V. P.; Langhammer, C. Grain boundary mediated hydriding phase transformations in individual polycrystalline metal nanoparticles. *Nat. Commun.* **2017**, *8* (1), 1084.

(52) Geng, X.; Li, S. W.; Heo, J.; Peng, Y.; Hu, W. H.; Liu, Y. C.; Huang, J. E.; Ren, Y.; Li, D. S.; Zhang, L.; et al. Grain-Boundary-Rich Noble Metal Nanoparticle Assemblies: Synthesis, Characterization, and Reactivity. *Adv. Funct. Mater.* **2022**, *32* (34), 2204169.

(53) Ostojic, N.; Crooks, R. M. Electrocatalytic Reduction of Oxygen on Platinum Nanoparticles in the Presence and Absence of Interactions with the Electrode Surface. *Langmuir* **2016**, *32* (38), 9727−9735.

(54) Song, M.; Zhou, G.; Lu, N.; Lee, J.; Nakouzi, E.; Wang, H.; Li, D. Oriented attachment induces fivefold twins by forming and

decomposing high-energy grain boundaries. *Science* **2020**, *367* (6473), 40.

(55) Padavala, S. K. M.; Nimasha, S.; Madhushani, K. A. U.; Luo, L.; Li, D.; Park, H.; Zhou, H.; Chen, N.; Pang, Q.; Sushko, P. V.; et al. Subsurface hydrogen, curvature, and strain: lessons from electroreduction of benzaldehyde on nano-structured Pd catalysts. *Journal of Materials Chemistry A* **2025**, *13*, 31770.

(56) Crespo-Quesada, M.; Andanson, J.-M.; Yarulin, A.; Lim, B.; Xia, Y.; Kiwi-Minsker, L. UV−Ozone Cleaning of Supported Poly(vinylpyrrolidone)-Stabilized Palladium Nanocubes: Effect of Stabilizer Removal on Morphology and Catalytic Behavior. *Langmuir* **2011**, *27* (12), 7909−7916.

(57) Zhang, D.; Jin, C.; Tian, H.; Xiong, Y.; Zhang, H.; Qiao, P.; Fan, J.; Zhang, Z.; Li, Z. Y.; Li, J. An In situ TEM study of the surface oxidation of palladium nanocrystals assisted by electron irradiation. *Nanoscale* **2017**, *9* (19), 6327−6333.

(58) Hÿtch, M. J.; Snoeck, E.; Kilaas, R. Quantitative measurement of displacement and strain fields from HREM micrographs. *Ultramicroscopy* **1998**, *74* (3), 131−146.

https://doi.org/10.1021/acs.nanolett.5c03431